



# Tabletop Testbed for Attitude Determination and Control of Nanosatellites

Rodrigo Cardoso da Silva<sup>1</sup>; Fernando Cardoso Guimarães<sup>2</sup>; João Victor Lopes de Loiola<sup>3</sup>; Renato Alves Borges, Ph.D.<sup>4</sup>; Simone Battistini, Ph.D.<sup>5</sup>; and Chantal Cappelletti, Ph.D.<sup>6</sup>

**Abstract:** To simulate the conditions of the space environment at ground, the Laboratory of Application and Innovation in Aerospace Science (LAICA) of the University of Brasília (UnB) is developing a dedicated testbed to reproducing nanosatellite attitude motion. The testbed is composed of an air-bearing table and a Helmholtz cage. The air-bearing table is a spacecraft simulator that can simulate frictionless conditions with three rotational degrees of freedom. Balancing the simulator is essential in order to make the gravitational torque negligible. The testbed is also equipped with a Helmholtz cage to recreate the Earth's magnetic field conditions that spacecrafts encounter in orbit. This paper presents the design and realization of this low-cost testbed. A simple and efficient automated balancing algorithm based on the least-squares method (LSM) is proposed and validated by experiments. The performance of the proposed simulator is evaluated and compared with previous works. DOI: [10.1061/\(ASCE\)AS.1943-5525.0000952](https://doi.org/10.1061/(ASCE)AS.1943-5525.0000952). © 2018 American Society of Civil Engineers.

## Introduction

Because of the great complexity and high budgets which usually accompany spacecraft projects, it is highly desirable to perform tests on ground-based platforms to reduce the risks. The effectiveness of performing tests on those platforms is closely related to their capacity to simulate the peculiarities of the space environment. For instance, the absence of atmosphere, the presence of microgravity, and the magnetic field of Earth are characteristics that directly affect the design of spacecraft attitude determination and control systems.

Since the beginning of the space race, air bearing-based platforms have been used as testbeds for simulating spacecraft attitude motion. Depending on the number of degrees of freedom (DOFs) provided, these platforms can be classified as planar, rotational, or combinational. Planar systems provide two translational degrees of freedom and, occasionally, a rotational degree of freedom (Schwartz et al. 2003).

This paper focuses on rotational systems, which aim to provide a frictionless rotational movement with three degrees of freedom. The inherent difficulty of this type of platform lies in achieving this rotational freedom, leading to some common build standards, such as tabletop, umbrella, and dumbbell (Schwartz et al. 2003). Because this paper uses the tabletop design, special attention is given to this configuration (Fig. 1). In this type of platform, the table is mounted directly on the air bearing. Although the rotational movement is constrained by the mounting plate and the hemisphere design, this is the most common design for rotational systems because it is easier to balance than are umbrella and dumbbell systems. Examples of tabletop designs were shown by Kim and Agrawal (2006) and Saulnier et al. (2013).

Combinational systems are those which combine the features of both planar and rotational systems. For this reason, these platforms often provide five to six degrees of freedom. Gallardo and Bevilacqua (2011) gave an example of a combinational system, a dynamic 6-DOF simulator. This platform was composed of two stages, one responsible for rotational motion and the other responsible for translational motion on an approximately 18 m<sup>2</sup> epoxy floor.

Common to all of these types of platform is the need for an efficient balancing procedure. The purpose of this balancing is to reduce the gravitational torque experienced by the platform. To accomplish this, the center of mass (CM) of the platform must be placed as close as possible to its center of rotation (CR), i.e., the unbalance vector magnitude must be as close as possible to zero. Mittelsteadt and Mehriel (2007) reported the importance of distributing the masses as symmetrically as possible and reserved space in the initial project for implementation of an automatic mass balancing system. This problem is often solved manually, as shown by Romano and Agrawal (2003) and Peck et al. (2003), in which a minimum gravitational torque of approximately 0.01 N · m was achieved. Carrara and Milani (2007) mentioned the need for balancing the system and described the adopted procedure for accomplishing it manually. There are also numerical algorithms that search for the optimal placement of each piece of equipment to be embedded in the platform (Xu et al. 2016). Carletta and Teofilatto (2017) addressed the necessity of implementing a balancing procedure. Thomas et al. (2018) presented the intent to

<sup>1</sup>Postgraduate Student, Dept. of Electrical Engineering, Univ. of Brasília, Campus Darcy Ribeiro, Brasília-DF CEP 70910-900, Brazil (corresponding author). Email: rcsilva@lara.unb.br

<sup>2</sup>Postgraduate Student, Dept. of Electrical Engineering, Univ. of Brasília, Campus Darcy Ribeiro, Brasília-DF CEP 70910-900, Brazil. Email: fguimaraes@lara.unb.br

<sup>3</sup>Postgraduate Student, Dept. of Electrical Engineering, Univ. of Brasília, Campus Darcy Ribeiro, Brasília-DF CEP 70910-900, Brazil. Email: victor@lara.unb.br

<sup>4</sup>Assistant Professor, Dept. of Electrical Engineering, Univ. of Brasília, Campus Darcy Ribeiro, Brasília-DF CEP 70910-900, Brazil. Email: raborges@ene.unb.br

<sup>5</sup>Assistant Professor, Faculty of Gama, Univ. of Brasília, Campus Gama, Gama-DF CEP 72444-240, Brazil. Email: simone.battistini@aerospace.unb.br

<sup>6</sup>Assistant Professor, Dept. of Mechanical, Materials, and Manufacturing Engineering, Univ. of Nottingham, Nottingham NG7 2RD, UK. Email: chantal.cappelletti@nottingham.ac.uk

Note. This manuscript was submitted on April 10, 2018; approved on June 18, 2018; published online on September 28, 2018. Discussion period open until February 28, 2019; separate discussions must be submitted for individual papers. This paper is part of the *Journal of Aerospace Engineering*, © ASCE, ISSN 0893-1321.

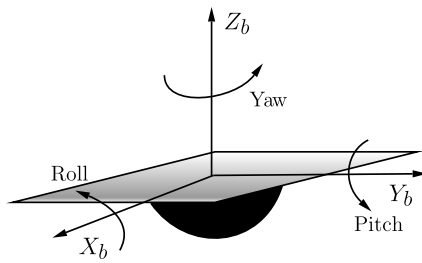


**Fig. 1.** Attitude angles in tabletop configuration.

implement a CubeSat simulator, similar to the one described in the present work. Moreover, the same balancing method described in the present work was the starting point for solving the balancing problem in Thomas et al. (2018), showing that this approach is being addressed in other facilities throughout the world.

Manual balancing procedures may take hours to obtain appropriate results. For this reason, other algorithms are based on automated processes, such as the algorithm presented by Kim and Agrawal (2009), which is an adaptive control scheme developed using Lyapunov theory. Other studies of adaptive control also use the unscented Kalman filter to tune the vertical component of the unbalance vector (Chesi et al. 2013).

This paper, in order to provide a cost-effective solution for the balancing problem, adapts the simple and efficient well-known least-squares method (LSM) to provide batch estimations of the unbalance vector of the platform (Silva et al. 2016).

This paper presents an attitude determination and control systems (ADCS) testbed composed of an air-bearing table and a Helmholtz cage being developed at the Laboratory of Application and Innovation in Aerospace Science (LAICA) of the University of Brasília. This platform is intended to simulate two key conditions present in the in-orbit environment: the magnetic field of the Earth and the frictionless conditions of rotations in space.

The air-bearing table is installed inside the Helmholtz cage, a device used to induce a magnetic field around the structure of the cage. In particular, inside the cage the induced magnetic field can be adjusted in order to recreate the Earth's magnetic field conditions that spacecraft encounter in orbit.

This paper is an extension of Silva et al. (2016). More experiments were run and further details were studied. This paper is divided as follows. The second section describes the air-bearing platform developed for testing nanosatellites, including an overview of its physical parts and the hardware/software architecture. A description of the assembly aspects involved with the project of the Helmholtz cage is also presented. The third section explains the balancing algorithm used and its theoretical foundations. The fourth section presents some tests conducted to evaluate the performance of the algorithm used to make the air-bearing table balancing. It also includes a comparative analysis with other balancing methods found in the literature. Conclusions are given in the fifth section.

## System Configuration

This section describes the components of the proposed testbed in two separate subsections. The first subsection addresses the constructive aspects of the hardware and the organization of the software of the air-bearing table. The second subsection presents the Helmholtz cage principle and describes its structure. The capability of magnetic field generation of the Helmholtz cage is illustrated with a set of measurements.

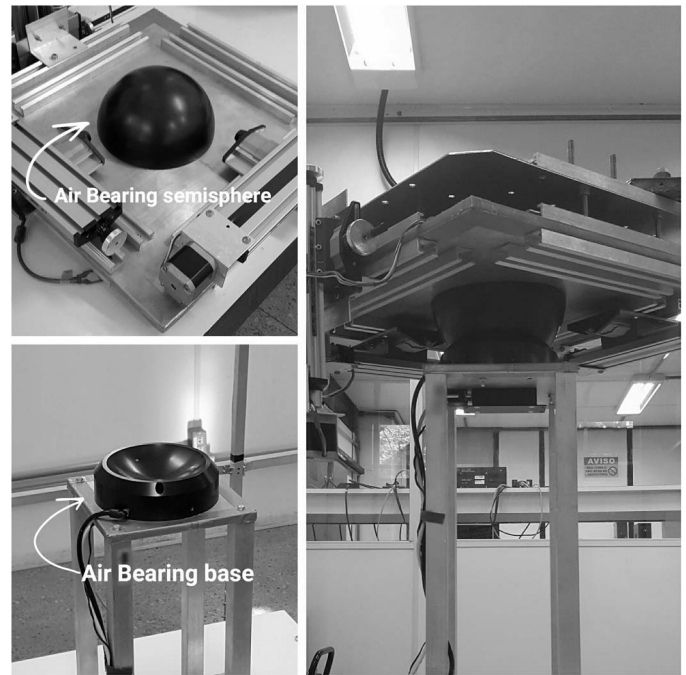


**Fig. 2.** Air-bearing assembly.

## Air-Bearing Table

The air-bearing table was conceived for testing attitude determination and control algorithms for nanosatellites. The air-bearing table developed at LAICA is an air-bearing platform in the tabletop configuration (Fig. 2) (Schwartz et al. 2003). In other words, the table is mounted directly on the semisphere of the air-bearing set. One major disadvantage of this configuration is the limitation of the extent of the roll and pitch angles, which will not exceed  $\pm 45^\circ$ . Nevertheless, this extent is sufficient for all the tests that will be conducted and, as is shown in section "Balancing Techniques," the full range is not required for the balancing algorithm to provide a consistent estimation of the unbalance vector.

The movable mass units (MMUs) (Fig. 3) are responsible for adjusting the position of the center of mass and have two degrees of freedom, although only one is used in each of the three MMUs. The two degrees of freedom of this device are accessible via a crank. To make this movement automatic and controllable by the electronic system, a motor is mounted in place of this crank for each MMU.

The electronic system embedded in the table contains

1. Microcontroller: a complete Universal Serial Bus (USB)-based microcontroller development system is implemented on an ATMEGA8 (Microchip, Chandler, Arizona) microcontroller. This platform, which is compatible with Arduino software and libraries, controls all the electronic components embedded in the balancing system of the air-bearing table.
2. Communication module: an XBee (Digi, Minnetonka, Minnesota) radio is used to make wireless communication with a computer that processes all the dynamic data collected.
3. Inertial measurement unit (IMU): an IMU with nine degrees of freedom is used, specifically a magnetometer with 3 DOFs, an accelerometer with 3 DOFs, and a gyroscope with 3 DOFs.
4. Motor drivers: three driver boards are used to control each of the three motors mounted on the table.
5. Stepper motors: three motors are mounted on the table. They make possible the translational movement of masses in three nonredundant degrees of freedom.
6. Batteries: two lithium polymer batteries power the system.

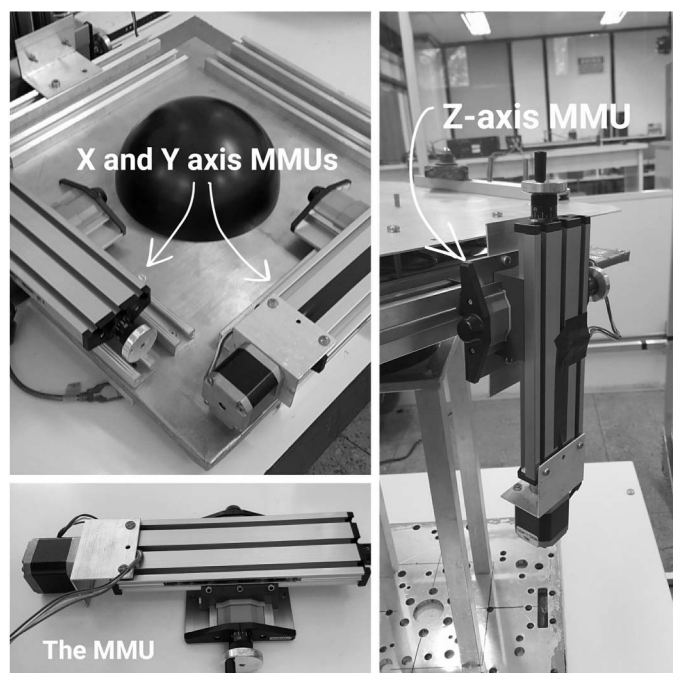


Fig. 3. Movable mass units.

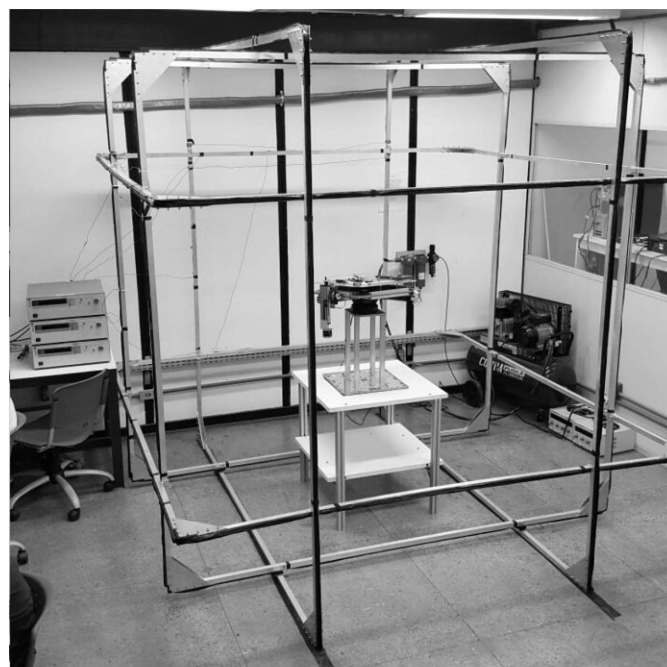


Fig. 5. Helmholtz cage. (Image by authors.)

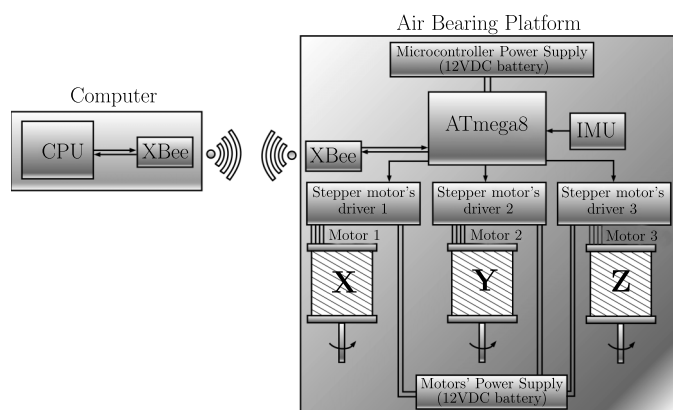


Fig. 4. Electronic components of system.

A schematic of the electronic system components is shown in Fig. 4.

### Helmholtz Cage

Control schemes based on magnetorquers must have a way to control the magnetic field of the test environment. To provide this capability, a Helmholtz cage was built.

The Helmholtz cage consists of a set of coils in which electric current runs in order to generate a magnetic field, as predicted by the Biot-Savart law of electromagnetics. By controlling the intensity and direction of this magnetic field, it is possible to simulate the orbital magnetic environment (Brewer 2012).

Six square coils, two for each axis of the cage, are used to generate an homogeneous field according to the applied electric current. The magnitude of the generated field is given, in each of the axes of the cage, by the following equation:

$$B = \frac{2\mu_0 NJ}{\pi a} \cdot \frac{2}{(1 + \gamma^2)\sqrt{2 + \gamma^2}} \quad (1)$$

where  $B$  = generated field;  $\mu_0$  = permeability of the environment;  $N$  = number of wire turns in the coil;  $J$  = applied current;  $a$  = half the side of the coil; and  $\gamma$  = relationship between the distance within two coils in a pair and the side of a coil, where in this case  $\gamma = 0.5445$ . Further details about Eq. (1) were given by Batista et al. (2018), who also clarified the definition of  $\gamma$ , an optimal construction parameter of the cage.

To manufacture this equipment, because the material used cannot possess magnetic characteristics, it was decided to use U-shaped aluminum profiles with 1 in. base, 1 in. side, and 3/32 in. thickness ( $1 \times 1 \times 3/32$ ). The bars are attached using triangular aluminum side supports and M5 stainless steel screws to build 2.5 m side squares. The structure is covered with enamelled copper wire, which constitutes the coil.

Once the structure is assembled, the coils are connected to a direct electrical current supply (DC) which feeds the system and generates the magnetic field. The current supply is automatically controlled through software compatible with MATLAB that interprets the readings from magnetometers mounted in the air-bearing table and calculates the current to be applied in order both to compensate the local magnetic field and establish the conditions suitable for the simulation of the orbital field needed. Fig. 5 shows the air-bearing platform surrounded by the Helmholtz cage.

Measurements taken with the maximum supply current of 6 A indicated that the cage is capable of generating approximately 180  $\mu\text{T}$  in each of its axes (Fig. 6). Fig. 6 shows the magnetic field in the laboratory environment with the Helmholtz cage turned off (initial portion of the graph) and with the cage turned on (final portion) in each axis. The environmental magnetic field is  $-26$ ,  $1.3$ , and  $18.05$   $\mu\text{T}$  in the  $x$ -,  $y$ -, and  $z$ -axes of the cage, respectively (Fig. 6). In other words, the cage is capable of nullifying the environmental magnetic field and still providing around 150  $\mu\text{T}$



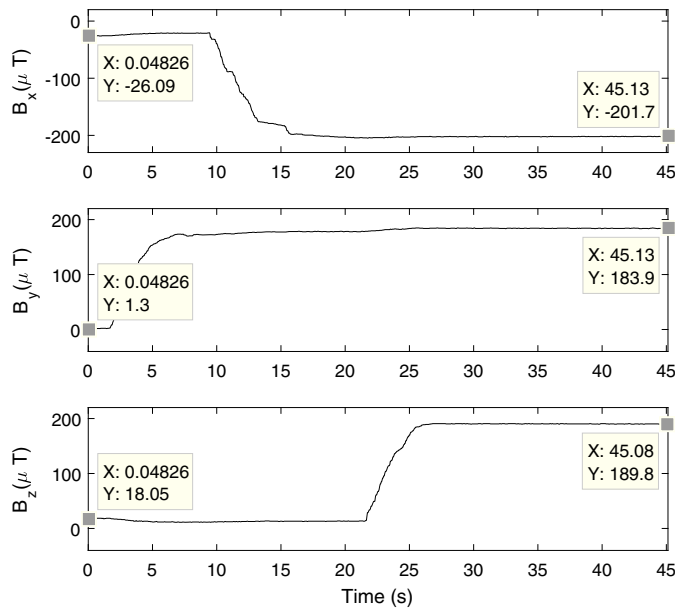


Fig. 6. Local magnetic field components measured at center of cage.

generation capability in each axis, which is sufficient for simulating most kinds of orbits. Another important aspect of the Helmholtz cage is the homogeneity of the magnetic field in its interior. The desired behavior of the generated magnetic field in a specific instant is that it must remain constant, in direction and magnitude, in a volume which must cover the air-bearing table entirely. de Loiola et al. (2018) conducted tests to quantify the homogeneity of the field generated by the Helmholtz cage described in this work, and concluded that the magnetic field remained constant, given some variation tolerance, along 100 cm of each cage axis. Because the air-bearing table, when rotating, occupies a volume of  $44 \times 44 \times 44$  cm, the homogeneity requisite is guaranteed.

## Balancing Techniques

### Reference Systems

Two reference systems were established for the air-bearing platform. The inertial frame, defined by the axes  $(X_i, Y_i, Z_i)$ , is static and fixed in relation with the laboratory; its origin is located at the CR of the air bearing. The body frame, defined by the axes  $(X_b, Y_b, Z_b)$ , is fixed in relation to the air-bearing table and moves with it; its origin is coincident with the origin of the inertial frame.

Fig. 7 illustrates the relative position between the inertial and body frames when the table performs a roll movement.

### Platform Dynamics

The platform can be modeled as a rigid body performing rotational movement and having its center of rotation fixed in both reference frames. For this system, the angular momentum taken at the center of rotation is given by (Greenwood 1988)

$$\mathbf{H}_{CR} = \mathbf{r} \times M\mathbf{v}_G + \mathbf{H}_G \quad (2)$$

where  $\mathbf{H}_G$  = angular momentum at the center of mass of the platform;  $M$  = total mass of the system;  $\mathbf{v}_G$  = velocity vector at the center of mass; and  $\mathbf{r}$  = CM offset, which is a vector starting from the CR and pointing to the CM.

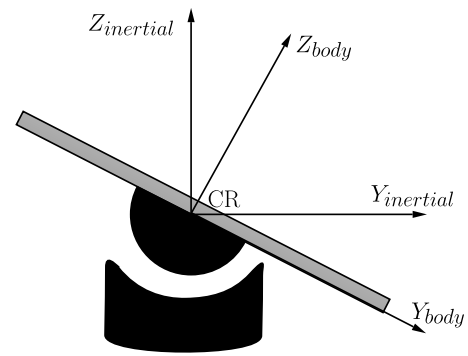


Fig. 7. Inertial and body frames during roll movement.

The system dynamics is obtained from Newton's second law, so that the torque applied to the system is equal to the time derivative of its angular momentum, that is

$$\boldsymbol{\tau}_{CR} = \frac{d\mathbf{H}_{CR}}{dt} \quad (3)$$

in which the resulting external torque,  $\boldsymbol{\tau}_{CR}$ , may take into account various torque effects, such as aerodynamic drag torque, actuation torque, and, mainly, the gravitational torque.

Evaluating the right-hand side of Eq. (3), with  $\mathbf{H}_{CR}$  given by Eq. (2), and taking into account the rate of change of vectors in rotating frames (Young 1998)

$$\frac{d\mathbf{H}_{CR}}{dt} = (\mathbf{r} \times M\dot{\mathbf{r}}) + [\boldsymbol{\omega} \times (\mathbf{r} \times M\dot{\mathbf{r}})] + \dot{\mathbf{H}}_G + (\boldsymbol{\omega} \times \mathbf{H}_G) \quad (4)$$

in which  $\boldsymbol{\omega}$  = angular velocity of body frame when rotating around the inertial frame. Eq. (4) can be written as

$$\mathbf{A} \cdot \dot{\boldsymbol{\omega}} + \mathbf{B} = \boldsymbol{\tau}_{CR} \quad (5)$$

in which the  $\mathbf{A} = \mathbf{A}(M, \mathbf{r}, \mathbf{I})$  and  $\mathbf{B} = \mathbf{B}(M, \mathbf{r}, \mathbf{I}, \boldsymbol{\omega})$  are  $3 \times 3$  and  $3 \times 1$  matrices, respectively; and  $\mathbf{I}$  = inertia tensor of the system.

The acceleration vector can be obtained from Eq. (5) as

$$\dot{\boldsymbol{\omega}} = (\mathbf{A})^{-1} \cdot (\boldsymbol{\tau}_{CR} - \mathbf{B}) \quad (6)$$

which can be solved simultaneously with the Euler angular rates to simulate the platform behavior.

### Dynamic Model Simplification

Subsection "Platform Dynamics" showed that the dynamics of the platform can be described by Eq. (6). Although this equation takes into account all the dynamic effects of the platform, its implementation is not the most cost-effective because some simplifications can be made without affecting the performance of the balancing algorithm. For instance, assuming that  $\boldsymbol{\omega}$  and  $\mathbf{r}$  in Eq. (6) have small magnitudes compared with the other terms, it follows that

$$\dot{\boldsymbol{\omega}} = (\mathbf{A})^{-1}(\boldsymbol{\tau}_{CR} - \mathbf{B}) \approx (\mathbf{I})^{-1} \cdot \boldsymbol{\tau}_{CR} \quad (7)$$

Additionally, assuming that the aerodynamic torque is negligible and considering null actuation torque, the resultant torque is given solely by the gravitational torque, thus  $\boldsymbol{\tau}_{CR} = \boldsymbol{\tau}_G$ .

This gravitational torque  $\tau_G$  can be determined by the cross product  $\tau_G = \mathbf{r} \times \mathbf{F} = \mathbf{r} \times M\mathbf{g}$ , in which  $\mathbf{F}$  is the moment force (weight) and  $\mathbf{g}$  is the local gravity vector.

Because all the vectors in the model must refer to the same reference system, the reference system fixed to the table (body frame) is chosen. Superscripts  $i$  and  $b$  are used to identify the quantities referred to the inertial and body frames, respectively. Consequently, the local gravity vector is given in the inertial frame as  $(\mathbf{g})^i = g \cdot [0 \ 0 \ -1]^T$ , in which  $g$  is a scalar with magnitude equal to the local gravity.

Using the Euler rotation matrix in the ZYX sequence that relates these two reference frames,  $\mathbf{R}_i^b$ , the local gravity can be described in the body frame as

$$(\mathbf{g})^b = \mathbf{R}_i^b \cdot (\mathbf{g})^i = \begin{bmatrix} g \cdot s_\theta \\ -g \cdot c_\theta s_\phi \\ -g \cdot c_\theta c_\phi \end{bmatrix} \quad (8)$$

in which the  $\phi$ ,  $\theta$ ,  $\psi$  notation is used for the roll, pitch, and yaw angles.

Then the gravitational torque may be calculated in the body frame as

$$\tau_G = \mathbf{r} \times M\mathbf{g} = Mg \begin{bmatrix} r_z c_\theta s_\phi - r_y c_\theta c_\phi \\ r_z s_\theta + r_x c_\theta c_\phi \\ -r_y s_\theta - r_x c_\theta s_\phi \end{bmatrix} \quad (9)$$

where scalars  $r_x$ ,  $r_y$ , and  $r_z$  = components of the unbalance vector  $\mathbf{r}$ .

Knowing that the inertia products have negligible magnitude compared with the principal moments

$$\mathbf{I} \approx \begin{bmatrix} I_{xx} & 0 & 0 \\ 0 & I_{yy} & 0 \\ 0 & 0 & I_{zz} \end{bmatrix} \Rightarrow \mathbf{I}^{-1} = \begin{bmatrix} \frac{1}{I_{xx}} & 0 & 0 \\ 0 & \frac{1}{I_{yy}} & 0 \\ 0 & 0 & \frac{1}{I_{zz}} \end{bmatrix} \quad (10)$$

Finally, substituting Eqs. (9) and (10) into Eq. (7), the dynamic model of the platform can be represented in a simplified manner as

$$\dot{\boldsymbol{\omega}} = \begin{bmatrix} \frac{Mg}{I_{xx}} (-r_y c_\phi c_\theta + r_z s_\phi c_\theta) \\ \frac{Mg}{I_{yy}} (r_x c_\phi c_\theta + r_z s_\phi s_\theta) \\ \frac{Mg}{I_{zz}} (-r_x s_\phi c_\theta - r_y s_\phi s_\theta) \end{bmatrix} \quad (11)$$

### Batch Estimation Balancing Algorithm

After mounting all the components described in section “System Configuration,” it was expected that the table would tend to reach an unbalanced position or, in other words, the table would be tilted (Fig. 8). Because the center of mass is displaced from the center of rotation of the table, a gravitational torque is produced around the CR which tilts the platform.

The gravitational torque experienced by the table interferes with the attitude control system of any nanosatellite placed on the table, therefore, it was necessary to minimize it. This gravitational torque was minimized by making the distance between the center of mass and the center of rotation of the table as close as possible to zero.

The proposed algorithm is as follows:

1. Dynamic data of the table are collected. These data are sent to the CPU through wireless communication. These data consist of the roll and pitch angles and the angular velocities of the table.
2. The CPU uses the data collected to estimate the distance between the CM and the CR of the table.
3. The CPU evaluates the required actuation, i.e., how much each motor will have to move, and sends this command to the air-bearing table through wireless communication.
4. After making the correction, dynamic data are collected again and the process is continued iteratively until the measured distance between the CR and the CM of the table reaches a pre-determined threshold.

Considering the simplified version of the dynamic model of the testbed given in Eq. (11), the least-squares method was used to improve the estimation of the components of the displacement vector (Young 1998). Eq. (11) can be integrated over a short period. In this way, the gyroscope data can be used and the only three unknowns that remain in this equation are the unbalance vector components. This assumes that the roll ( $\phi$ ) and pitch ( $\theta$ ) angles are almost constant during a small time step. The result is

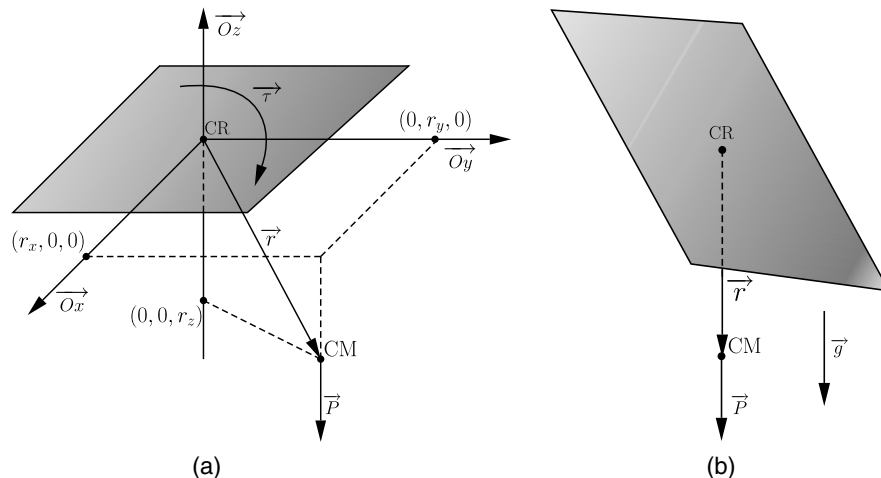


Fig. 8. Effect of gravitational torque: platform before and after reaching equilibrium.

$$\begin{aligned}
(\Delta\omega_x)_{t_2-t_1} &= \frac{-Mg\Delta t}{2I_{xx}} \left\{ \left[ (c_\phi c_\theta)_{t_2} + (c_\phi c_\theta)_{t_1} \right] r_y \right. \\
&\quad \left. - \left[ (s_\phi c_\theta)_{t_2} + (s_\phi c_\theta)_{t_1} \right] r_z \right\} \\
(\Delta\omega_y)_{t_2-t_1} &= \frac{Mg\Delta t}{2I_{yy}} \left\{ \left[ (c_\phi c_\theta)_{t_2} + (c_\phi c_\theta)_{t_1} \right] r_x \right. \\
&\quad \left. + \left[ (s_\theta)_{t_2} + (s_\theta)_{t_1} \right] r_z \right\} \\
(\Delta\omega_z)_{t_2-t_1} &= \frac{-Mg\Delta t}{2I_{zz}} \left\{ \left[ (s_\phi c_\theta)_{t_2} + (s_\phi c_\theta)_{t_1} \right] r_x \right. \\
&\quad \left. + \left[ (s_\theta)_{t_2} + (s_\theta)_{t_1} \right] r_y \right\}
\end{aligned} \quad (12)$$

which can be rewritten as

$$\underbrace{\begin{bmatrix} \Delta\omega_x \\ \Delta\omega_y \\ \Delta\omega_z \end{bmatrix}}_{\Delta\Omega} = \underbrace{\begin{bmatrix} 0 & \phi_{12} & \phi_{13} \\ \phi_{21} & 0 & \phi_{23} \\ \phi_{31} & \phi_{32} & 0 \end{bmatrix}}_{\Phi} \cdot \underbrace{\begin{bmatrix} r_x \\ r_y \\ r_z \end{bmatrix}}_{\mathbf{r}} \quad (13)$$

where the  $\phi_{ij}$  terms are given as

$$\begin{aligned}
\phi_{12} &= -\frac{Mg\Delta t}{2I_{xx}} \left[ (c_\phi c_\theta)_{t_2} + (c_\phi c_\theta)_{t_1} \right] \\
\phi_{13} &= \frac{Mg\Delta t}{2I_{xx}} \left[ (s_\phi c_\theta)_{t_2} + (s_\phi c_\theta)_{t_1} \right] \\
\phi_{21} &= \frac{Mg\Delta t}{2I_{yy}} \left[ (c_\phi c_\theta)_{t_2} + (c_\phi c_\theta)_{t_1} \right] \\
\phi_{23} &= \frac{Mg\Delta t}{2I_{yy}} \left[ (s_\theta)_{t_2} + (s_\theta)_{t_1} \right] \\
\phi_{31} &= -\frac{Mg\Delta t}{2I_{zz}} \left[ (s_\phi c_\theta)_{t_2} + (s_\phi c_\theta)_{t_1} \right] \\
\phi_{32} &= -\frac{Mg\Delta t}{2I_{zz}} \left[ (s_\theta)_{t_2} + (s_\theta)_{t_1} \right]
\end{aligned} \quad (14)$$

The LSM method is used because it finds a suitable estimation of the solution using all the data acquired from the sensors over time. It is also useful to prevent the occurrence of gross errors in the estimation caused by any kind of instantaneous sensor failure, because the estimation will not be evaluated using data of only one instant. Oversampling Eq. (13) results in the following system:

$$\underbrace{\begin{bmatrix} (\Delta\omega_x)_{t_0} \\ (\Delta\omega_y)_{t_0} \\ (\Delta\omega_z)_{t_0} \\ (\Delta\omega_x)_{t_1} \\ (\Delta\omega_y)_{t_1} \\ (\Delta\omega_z)_{t_1} \\ \vdots \end{bmatrix}}_{\Delta\Omega_L} = \underbrace{\begin{bmatrix} 0 & (\phi_{12})_{t_0} & (\phi_{13})_{t_0} \\ (\phi_{21})_{t_0} & 0 & (\phi_{23})_{t_0} \\ (\phi_{31})_{t_0} & (\phi_{32})_{t_0} & 0 \\ 0 & (\phi_{12})_{t_1} & (\phi_{13})_{t_1} \\ (\phi_{21})_{t_1} & 0 & (\phi_{23})_{t_1} \\ (\phi_{31})_{t_1} & (\phi_{32})_{t_1} & 0 \\ \vdots & \vdots & \vdots \end{bmatrix}}_{\Phi_L} \cdot \underbrace{\begin{bmatrix} r_x \\ r_y \\ r_z \end{bmatrix}}_{\mathbf{r}} \quad (15)$$

which can be solved using the LSM providing the displacement vector

$$\mathbf{r} = [\Phi_L^T \cdot \Phi_L]^{-1} \cdot \Phi_L^T \cdot \Delta\Omega_L \quad (16)$$

After properly estimating the distance between the CR and the CM, the actuation system is responsible for compensating the

unbalanced vector components. Assuming that all MMUs displace the same amount of mass in each of the three nonredundant translational degrees of freedom of the table, the actuation parameters are given by

$$\Delta \mathbf{r}_{\text{MMU}} = -\frac{M}{m_{\text{MMU}}} \cdot \mathbf{r}_{\text{CM}} \quad (17)$$

### Variation of Inertia Tensor

The inertia parameters of the platform are used in Eq. (16) to determine the unbalance vector components. These parameters are estimated in CAD software and used to start the algorithm. For the current configuration of the platform, the inertia tensor is given by

$$\mathbf{I} = \begin{bmatrix} I_{xx} & I_{xy} & I_{xz} \\ I_{yx} & I_{yy} & I_{yz} \\ I_{zx} & I_{zy} & I_{zz} \end{bmatrix} = \begin{bmatrix} 0.265 & -0.014 & -0.035 \\ -0.014 & 0.246 & -0.018 \\ -0.035 & -0.018 & 0.427 \end{bmatrix} [\text{kg} \cdot \text{m}^2] \quad (18)$$

and, as expected, the inertia products have much smaller magnitudes than the principal moments of inertia. After each movement of a MMU, this initial inertia tensor is changed. These changes may be tracked in each iteration and incorporated to the algorithm to make corrections of the inertia tensor (Kim and Agrawal 2009).

### Simulation and Tests

The tests conducted in this paper illustrate the quality of the balancing procedure based on batch estimation. By comparing the period of the platform oscillation with that of a simple pendulum, it was possible to show the improvement of the results after each interaction of the balancing algorithm. Another way of verifying the balancing performance is to register the initial and final positions of the platform. Starting from a tilted position, the platform should conclude the balancing procedure in an almost horizontal position as the roll and pitch angles of the platform became approximately null. However, the roll and pitch angles are expected to diminish to zero only in the case that the magnitude of the unbalance vector in the  $Z_b$  axis stays much higher than the magnitude of the horizontal plane component of the unbalance vector. Otherwise, the table could reach any other final inclination.

This points to a limitation of the balancing capability in the vertical axis ( $Z_b$ ). Although the  $X_b$  and  $Y_b$  components become well balanced, a considerable unbalance remains in the vertical axis of the platform because there is much more mass concentrated below its CR. There are several ways to avoid this problem, for instance, increasing the mass that each MMU can move or simply adding more weight above the CR of the platform. In this project, it was decided to let the  $Z_b$  component of the unbalance vector to reach larger values by implementing an interface for mounting hardware above the initial configuration of the platform. The height of this plate related to the table is adjustable with screws.

This enabled the balancing process to position the CM even closer to the CR (Fig. 9). In addition, the final period of oscillation of the table in the roll and pitch axes increased to 22.83 and 20.81 s, respectively. In these new results, the MMUs were allowed to move a fixed maximum in each iteration, in order to better track the evolution of the unbalance vector. Table 1 presents the period of oscillation of the pitch axis starting from an arbitrary unbalance condition in which the MMUs were positioned randomly. The estimates of the unbalance vector components at

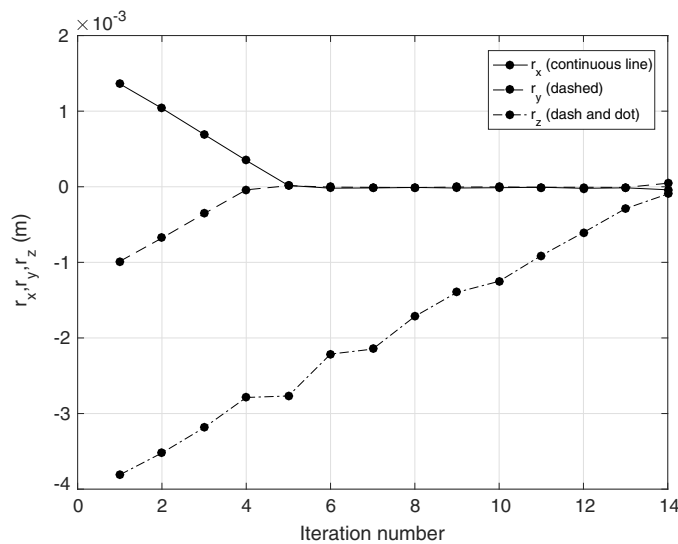


**Fig. 9.** Evolution of  $\mathbf{r}$  components during balancing after increasing mass above CR.

the end of the balancing procedure were, for the  $X_b$ ,  $Y_b$ , and  $Z_b$  axes,  $-14.1$ ,  $-9.0$ , and  $-288.9 \mu\text{m}$ , respectively. The  $Z_b$  component did not achieve a magnitude similar to that obtained in the  $X_b$  and  $Y_b$  axes, because the balancing procedure stopped in order to guarantee a stable position of the table, avoiding inverted pendulum behavior. This behavior is characterized by the positioning of the CM above the CR, which makes the testbed move to the roll/pitch limits.

Each MMU has a total extent of 134 mm. Each complete turn performed by the stepper motor on the crank of the MMU displaces a mass of approximately 0.7 kg by exactly 1 mm in the direction of the associate axis. Because the stepper motor driver is configured in the 200-step mode, each turn corresponds to 200 voltage pulses sent to the driver. In other words, it is possible to perform just 1/200 of a turn by sending a single pulse to the motor, meaning a displacement of 5/1,000 mm of the movable mass. The unbalance vector variation  $\Delta\mathbf{r}$  is

$$\Delta\mathbf{r} = \frac{m_{\text{MMU}}}{M} \begin{bmatrix} r_{mx} \\ r_{my} \\ r_{mz} \end{bmatrix} \quad (19)$$

**Table 1.** Oscillation period during balancing procedure (table with mounting plate)

Iteration number	$\ \mathbf{r}\ $ ( $\mu\text{m}$ )	Oscillation period	
		Calculated (s)	Measured (s)
Initial condition	4,164.75	4.0827	4.3200
1	3,732.98	4.3124	4.7041
2	3,280.38	4.6003	4.7204
3	2,809.32	4.9710	5.4423
4	2,767.58	5.0084	5.5081
5	2,213.58	5.6002	5.8774
6	2,147.67	5.6855	6.2218
7	1,715.05	6.3622	6.9219
8	1,396.50	7.0506	7.7607
9	1,250.46	7.4510	8.5203
10	910.12	8.7337	10.0773
11	605.13	10.7108	12.9215
12	289.42	15.4876	20.8118

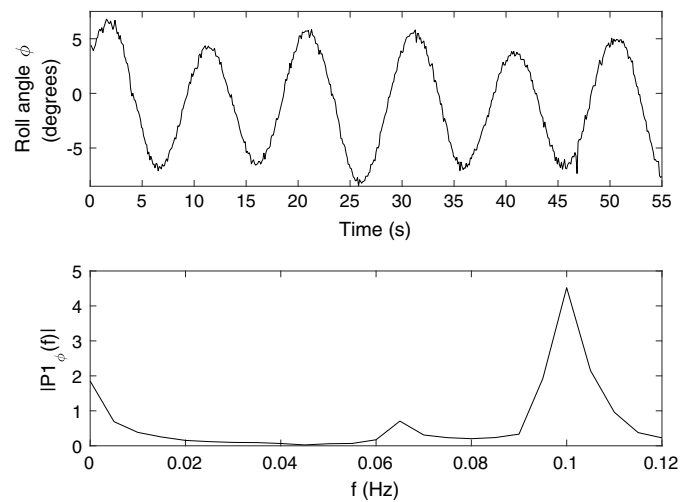


**Fig. 10.** Roll angle and corresponding frequency spectrum at third iteration of balancing procedure.

where  $r_{mi}$ ,  $i \in \{x, y, z\}$  = displacements performed by each movable mass. Because the testbed developed in this work weighs 14 kg, Eq. (19) implies that the minimum change in any component of the unbalance vector  $\mathbf{r}$  is  $0.25 \mu\text{m}$ , whereas the maximum change is 6.7 mm. This range determines the maximum unbalance that can be compensated, as well as how close to the origin the MMUs can place the unbalance vector, which is in accordance with the initial and final values of  $\|\mathbf{r}\|$  in Table 1. A  $0.25\text{-}\mu\text{m}$  minimum step may indicate that a minimum of  $3.5 \times 10^{-5} \text{ N} \cdot \text{m}$  gravitational torque is reachable [Eq. (9)]. However, some obstacles, such as the noise level of the sensor measurements, make it impossible for the gravitational torque to reach this minimum gravitational torque level, as is mentioned subsequently.

Alternatively to the inspection method for estimating the oscillation period of the platform, in which the time difference between two peaks is measured, it is possible to analyze the frequency spectrum of these signals. In a second balancing test, the platform was first manually prebalanced and three iterations of the balancing algorithm were executed. Applying the fast Fourier transform (FFT) to the oscillation signal obtained in the third iteration, it was possible to identify three main frequency components (Fig. 10). One is a constant component related to the steady-state equilibrium point of the platform, and the other two components are related to the pendulum dynamics of the platform. The presence of two frequency components different from 0 instead of 1 is related to the energy exchange between the roll and pitch axes. The spectrum component of 0.1 Hz is dominant (Fig. 10), which is also determined by checking the period of the signal in the time domain.

These results show that the proposed balancing method provides adequate balancing performance. As a means of comparison, the values obtained for the  $x$ - and  $y$ -components present the same order of magnitude of similar works, such as Liu et al. (2016), which reached a range of  $5 \mu\text{m}$  for the unbalance vector magnitude.

Additionally, the convergence of the unbalance vector was also analyzed, similarly to Young (1998). This analysis is important to define the minimum required length in order to provide good estimations of the unbalance vector. The platform was excited with an initial angular momentum and sensor data were acquired during 5 min at a sampling frequency of 10 Hz. Then the unbalance vector norm was calculated with various lengths of data, as well as the corresponding standard deviation. Fig. 11 shows the initial 50 s of this graph. The five initial samples of the estimated unbalance



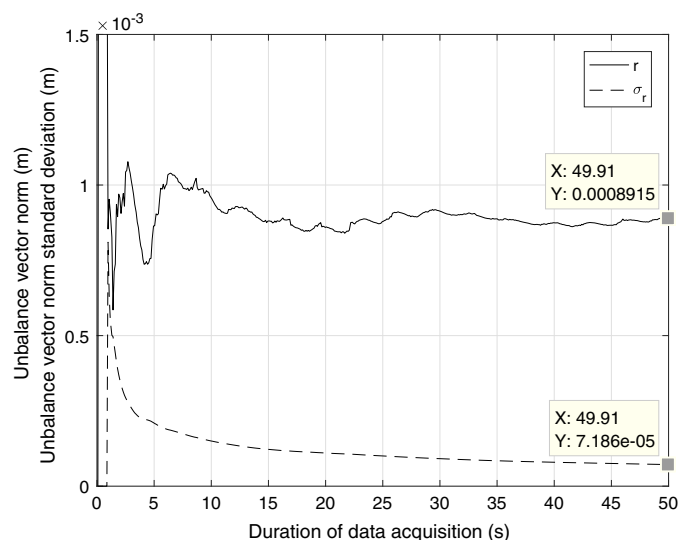


**Fig. 11.** Analysis of the LSM method convergence.

vector norm were not considered for the determination of the standard deviation graph, because they introduced considerable bias. The tests show that after 5 s there was already an expressive decay in the standard deviation of the norm estimation, and after 40 s, changes in the unbalance vector norm were minimal. In other words, 40 s of data acquisition at 10 Hz is proved to be enough for a reasonably good estimation of the unbalance vector in the proposed tabletop testbed. Furthermore, the value to which the standard deviation converges, about  $0.2 \mu\text{m}$  (Fig. 11), indicates the minimum trustworthy estimate of the unbalance vector and is related to the noise level in the IMU measurements.

Other balancing algorithms by Kim and Agrawal (2009) and Chesi et al. (2013) could also be implemented in the proposed platform. However, the results by Kim and Agrawal (2009) were based on an adaptive control method that cannot be tested in a platform equipped with balancing masses only, and Kim and Agrawal (2009) used control moment gyros (CMGs), which are responsible for tracking a particular angular momentum trajectory and use the error as feedback to the adaptive control algorithm.

In this work, similarly to Chesi et al. (2013), the only source of control torque was that provided by the moving masses.

Consequently, these torques are perpendicular to the gravity field. To avoid this restriction of generating torque in the vertical axis, a two-stage balancing algorithm was developed in which, in the first stage, only the unbalance vector components in the transverse plane are compensated using the adaptive feedback control law. Then, in a second stage, an unscented Kalman filter is used to compensate for the last unbalance vector component, which is parallel to the gravity field.

In this work, the main limitation of implementing the adaptive control scheme developed by Kim and Agrawal (2009) is the absence of an alternative control torque source, whereas, for the two-stage scheme developed by Chesi et al. (2013), the bottleneck is the processing capacity of the adopted microcontroller. Both strategies use an onboard computer with high processing capacity, different from the commercial off-the-shelf (COTS) microcontroller used in this work, which is overwhelmed with the batch estimation implementation, even though the LSM data are processed in an external computer.

The sensor performance must be also analyzed. Kim and Agrawal (2009) mentioned that the tracking errors used as feedback tend to zero when there are no external torque disturbances. However, the momentum tracking errors are noisy when the angular measurements are noisy. Thus, the mass balancing accuracy is highly sensitive to the quality of the sensor in this balancing method. In fact, a comparison of the batch estimation and the adaptive control by Kim and Agrawal (2009) showed that, for some cases, the gravitational disturbances were better diminished with batch estimation, and when the adaptive control presented better results, the improvement was only about 46% at best. Section "System Configuration" showed that the gyroscope measurement resolution provided by the IMU is  $0.01 \text{ rad/s}$  or, equivalently,  $0.5730^\circ/\text{s}$ , much less than that provided by the IMU700 inertial measurement unit used by Kim and Agrawal (2009), which was less than  $0.025^\circ/\text{s}$  (more than 23 times better). Consequently, it is expected, a priori, that the implementation of the Kim and Agrawal method in this work would produce even worse results. Chesi et al. (2015) also mentioned the influence of unmodeled noise effects in the measurements of the IMU. In this case, the IMU used, an ADIS16400 (Analog Devices, Norwood, Massachusetts), provided  $0.05^\circ/\text{s}$  of resolution. The advantages and disadvantages of each balancing method are summarized in Table 2.

In this context, the batch estimation method proved to be adequate in a low-cost system in which the sensor data may not have

**Table 2.** Pros and cons of each balancing method

Pro/con	Description
Silva et al. (2016)	
Pros	Satisfactory results are obtained using a low-complexity algorithm. Does not require CMGs. Actuation uses movable masses only. Less sensitivity to sensor quality, because the noise effect is minimized by the least-squares method. Does not require an embedded controller, because calculations may be made in an external computer (consequently, there is no need for high processing capacity embedded in the onboard computer).
Cons	Does not solve the inverted pendulum problem. Correctness of the method is highly dependent on the accurate estimation of the inertia tensor. Method must be repeated several times until good balancing is achieved. Other methods may achieve better results.
Chesi et al. (2013)	
Pros	Does not require CMGs. Actuation uses movable masses only. Capable of obtaining better results than those obtained with batch estimation.
Cons	Does not solve the inverted pendulum problem. Sensitive to noise presence or low resolution in sensor measurements, in which case the batch estimation may obtain better results.
Kim and Agrawal (2009)	
Pros	Solves the inverted pendulum problem. Capable of obtaining better results than those obtained with batch estimation.
Cons	Sensitive to noise presence or low resolution in sensor measurements, in which case the batch estimation may obtain better results. Requires CMGs, i.e., active torque actuators.



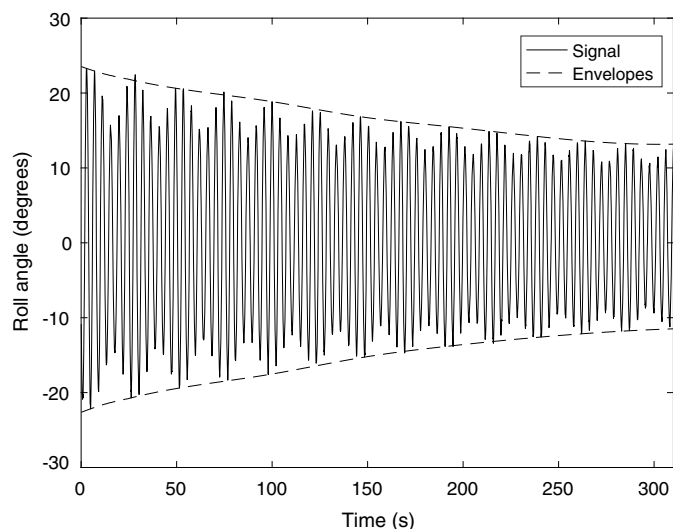


**Fig. 12.** Influence of aerodynamic drag on roll angle amplitude.

the desired precision. The LSM method, when applied with enough data, may suppress the noise influence.

Furthermore, the platform oscillation decays with time, although it is assumed that there is no friction in the air bearing (Fig. 12). This occurs because the aerodynamic drag torque, in fact, is present. Because this effect is not predicted in the model simplification in Eq. (11), it may cause deviations in the unbalance vector estimation provided by the LSM method if data are collected for a long time. In other words, there is a trade-off between the estimation convergence and its precision. The aerodynamic drag problem was also addressed by Chesi et al. (2013).

## Conclusions

This paper described a new platform developed at the University of Brasília for testing attitude determination and control systems of nanosatellites. The platform simulates the attitude dynamics of nanosatellites by using an air-bearing table.

A LSM procedure was proposed, based on data from a COTS IMU, to reduce the distance between the center of mass and the center of rotation of the air-bearing table. A set of movable masses attached to the table are moved in accordance with the LSM algorithm, and this allows the balancing of the platform. Results showed that, although only low-cost COTS electronic devices were used, the performance of the balancing system is satisfactory, because the achieved unbalance range is compatible with that in other works.

The testbed also includes a Helmholtz cage. The association between the testbed and the Helmholtz cage extends the range of simulation possibilities by making possible the simulation of the magnetic field of the Earth. Measurements taken during its operation showed that the cage is capable of generating enough magnetic field to run and test magnetic control algorithms, which will be done in future work.

## Acknowledgments

This work was supported by the University of Brasília (UnB), the Federal District Research Support Foundation (FAPDF), the Coordination for the Improvement of Higher Education

Personnel (CAPES), and the National Council for Scientific and Technological Development (CNPq).

## Notation

The following symbols are used in this paper:

- $a$  = length of half the side of the coil (m);
- $b$  = superscript of variables related to the body frame;
- $c$  = cosine of angle variable denoted by  $\bullet$ ;
- $G$  = subscript related to gravity field or vectors applied to the CM;
- $g$  = magnitude of local gravity vector;
- $\mathbf{H}$  = vector of angular momentum;
- $\mathbf{I}$  = inertia tensor;
- $I_{ij}$  = components of inertia tensor,  $i, j \in \{x, y, z\}$ ;
- $i$  = superscript of variables related to inertial frame;
- $J$  = applied current in coil (A);
- $L$  = length of the pendulum rod (m);
- $M$  = total mass of the platform (kg);
- $m$  = mass (kg);
- $\mathbf{R}_i^j$  = rotation matrix in  $i, j$  reference frames;
- $\mathbf{r}$  = unbalance vector or CM vector;
- $s$  = sine of angle variable denoted by  $\bullet$ ;
- $T$  = oscillation period (s);
- $t_i$  = subscript that denotes variable taken at time  $t_i$ ;
- $\mathbf{v}$  = vector of linear velocity;
- $x, y, z$  = subscripts used to denote scalar quantities related to the  $x$ -,  $y$ -, and  $z$ -axis, respectively;
- $\times$  = standard cross product for vectors in  $\mathbb{R}^3$ ;
- $\gamma$  = aerodynamic coefficient of platform;
- $\theta$  = pitch angle (rad);
- $\tau$  = torque ( $\text{N} \cdot \text{m}$ );
- $\phi$  = roll angle (rad);
- $\psi$  = yaw angle (rad); and
- $\boldsymbol{\omega}$  = vector of angular velocities (rad/s).

## References

- Batista, D. S., F. Granziera, M. C. Tosin, and L. F. de Melo. 2018. "Three-axial Helmholtz coil design and validation for aerospace applications." *IEEE Trans. Aerosp. Electron. Syst.* 54 (1): 392. <https://doi.org/10.1109/TAES.2017.2760560>.
- Brewer, M. R. 2012. "CubeSat attitude determination and Helmholtz cage design." M.S. thesis, Dept. of Aeronautics and Astronautics, Air Force Institute of Technology.
- Carletta, S., and P. Teofilatto. 2017. "Design and development of a full 5-DOF testbed for testing nanosatellites formation flying, rendezvous and proximity operations." In *Proc., 9th Int. Workshop on Satellite Constellations and Formation Flying*. Boulder, CO: Univ. of Colorado Boulder.
- Carrara, V., and P. G. Milani. 2007. "Controle de uma mesa de mancal a ar de um eixo equipada com giroscópio e roda de reação." In *V SBEIN-Simpósio Brasileiro de Engenharia Inercial*, 26–29. Rio de Janeiro, Brazil: Military Institute of Engineering.
- Chesi, S., Q. Gong, V. Pellegrini, R. Cristi, and M. Romano. 2013. "Automatic mass balancing of a spacecraft three-axis simulator: Analysis and experimentation." *J. Guidance Control Dyn.* 37 (1): 197–206. <https://doi.org/10.2514/1.60380>.
- Chesi, S., O. Perez, and M. Romano. 2015. "A dynamic, hardware-in-the-loop, three axis simulator of spacecraft attitude maneuvering with nanosatellite dimensions." *J. Small Satellites* 4 (1): 315–328.
- de Loiola, J. V. L., L. C. van der Ploeg, R. C. da Silva, F. C. Guimarães, R. A. Borges, and G. A. Borges. 2018. "3 axis simulator of the earth

- magnetic field.” In *Proc., 39th IEEE Aerospace Conf.*, 1–8. Piscataway, NJ: IEEE.
- Gallardo, D., and R. Bevilacqua. 2011. “Six degrees of freedom experimental platform for testing autonomous satellites operations.” In *Proc., 8th Int. ESA Conf. on Guidance, Navigation and Control Systems*, 1–11. Paris: European Space Agency.
- Greenwood, D. T. 1988. *Principles of dynamics*. Englewood Cliffs, NJ: Prentice-Hall.
- Kim, J. J., and B. N. Agrawal. 2009. “Automatic mass balancing of air-bearing-based three-axis rotational spacecraft simulator.” *J. Guidance Control Dyn.* 32 (3): 1005–1017. <https://doi.org/10.2514/1.34437>.
- Kim, J.-J., and B. N. Agrawal. 2006. “System identification and automatic mass balancing of ground-based three-axis spacecraft simulator.” In *Proc., AIAA Guidance Navigation and Control Conf. and Exhibit*, 1–12. Reston, VA: AIAA.
- Liu, Y., L. Li, Z. Fu, J. Tan, and K. Li. 2016. “Automatic mass balancing of a spacecraft simulator based on non-orthogonal structure.” In *Proc., 2016 UKACC 11th Int. Conf. on Control (CONTROL)*, 1–6. Piscataway, NJ: IEEE.
- Mittelsteadt, C., and E. Mehiel. 2007. “Cal Poly spacecraft attitude dynamics simulator: CP/SADS.” In *Proc., AIAA Guidance, Navigation and Control Conf. and Exhibit*, 1–24. Reston, VA: AIAA.
- Peck, M. A., L. Miller, A. R. Cavender, M. Gonzalez, and T. Hintz. 2003. “An airbearing-based testbed for momentum control systems and spacecraft line of sight.” *Adv. Astronaut. Sci.* 114: 427–446.
- Romano, M., and B. N. Agrawal. 2003. “Acquisition, tracking and pointing control of the bifocal relay mirror spacecraft.” *Acta Astronaut.* 53 (4): 509–519. [https://doi.org/10.1016/S0094-5765\(03\)80011-5](https://doi.org/10.1016/S0094-5765(03)80011-5).
- Saulnier, K., D. Perez, G. Tilton, D. Gallardo, C. Shake, R. Huang, and R. Bevilacqua. 2013. “Operational capabilities of a six degrees of freedom spacecraft simulator.” In *Proc., AIAA Guidance, Navigation, and Control (GNC) Conf.*, 5253. Reston, VA: AIAA.
- Schwartz, J. L., M. A. Peck, and C. D. Hall. 2003. “Historical review of air-bearing spacecraft simulators.” *J. Guidance Control Dyn.* 26 (4): 513–522. <https://doi.org/10.2514/2.5085>.
- Silva, R. C., U. A. Rodrigues, R. A. Borges, M. Sampaio, P. Beghelli, S. G. P. Costa, B. T. Popov, S. Battistini, and C. Cappelletti. 2016. “A testbed for attitude and determination control of spacecrafts.” In *Proc., II IAA Latin American Cubesat Workshop*. Paris: International Academy of Astronautics.
- Thomas, D., A. T. Wolosik, and J. Black. 2018. “CubeSat attitude control simulator design.” In *Proc., 2018 AIAA Modeling and Simulation Technologies Conf.*, 1391. Reston, VA: AIAA.
- Xu, Z., Y. Chen, N. Qi, Q. Sun, Y. Fan, and C. Wang. 2016. “Inertia parameters optimisation method for three-axis spacecraft simulator.” *Electron. Lett.* 52 (20): 1675–1677. <https://doi.org/10.1049/el.2016.1660>.
- Young, J. S. 1998. “Development of an automatic balancing system for a small satellite attitude control simulator.” M.S. thesis, Dept. of Mechanical Engineering, Utah State Univ.